**Proceedings of IDETC/CIE 2005**
**ASME 2005 International Design Engineering Technical Conferences**
**& Computers and Information in Engineering Conference**
**September 24-28, 2005, Long Beach, California USA**

**DETC2005-85092**

# A HYBRID ROD-CATENARY MODEL TO SIMULATE NONLINEAR DYNAMICS OF CABLES WITH LOW AND HIGH TENSION ZONES

**S. Goyal**
Student Member, ASME
University of Michigan, Mechanical Engineering
2350 Hayward, Ann Arbor, Michigan-48109-2125, U.S.
Email. sgoyal@umich.edu

**N. C. Perkins**
Fellow, ASME
University of Michigan, Mechanical Engineering
2350 Hayward, Ann Arbor, Michigan-48109-2125, U.S.
Email. ncp@umich.edu

## ABSTRACT

Cables under very low tension may become highly contorted and form loops, tangles, knots and kinks. These nonlinear deformations, which are dominated by flexure and torsion, pose serious concerns for cable deployment. Simulation of the three-dimensional nonlinear dynamics of loop and tangle formation requires a $12^{th}$ order rod model and the computational effort increases rapidly with increasing cable length and integration time. However, marine cable applications which result in local zones of low-tension very frequently involve large zones of high-tension where the effects of flexure and torsion are insignificant. Simulation of the three-dimensional dynamics of high-tension cables requires only a $6^{th}$ order catenary model which significantly reduces computational effort relative to a rod model. We propose herein a hybrid computational cable model that employs computationally efficient catenary elements in high-tension zones and rod elements in localized low-tension zones to capture flexure and torsion precisely where needed.

**Keywords:** rod, catenary, cable, dynamics

## 1. INTRODUCTION

Marine cables tend to form loops and tangles in low tension zones due to combined effects of residual torsion and flexure. This loading scenario is often realized on the seabed as illustrated in Fig. 1. In this context, loops are often termed "hockles" and these can hinder cable laying and recovery operations, attenuate signal transmission in fiber-optic cables, and can even lead to the formation of knots and kinks that damage cables.

The large nonlinear deformations associated with loop formation are dominated by flexure and torsion, effects that are not captured in models that treat the cable as perfectly flexible. To capture these effects, one must treat the cable as a rod-like element following, for example, the classical rod theory of Kirchhoff/Clebsch [1]. Modern treatments and advancements in rod theories are comprehensively summarized by Antman [2]. Loop formation in elastic rods may be initiated by elastic instabilities under compression and/ or torsion; refer, for example, to the buckling conditions developed by Greenhill [3] or Zachman [4].

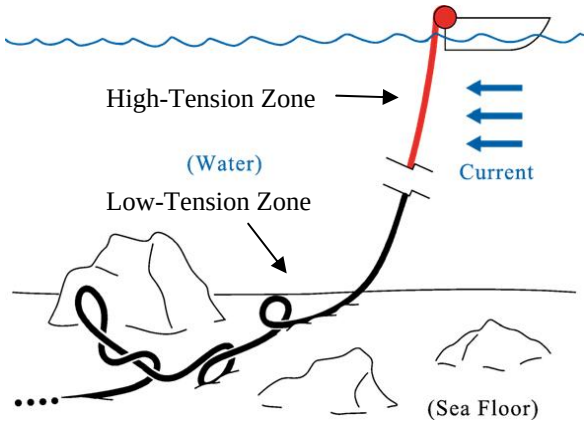


**Fig. 1**: Cable forming loops and tangles on the sea floor.

Rod theories have been used to model the mechanics of cables starting with the work of Zajac [5] who studied the onset of "pop-out" instabilities in planar loops using equilibrium rod theory. His work on the nonlinear equilibria of rods has been extended [6-9] to further investigate loop formation and "pop-out" instabilities under a variety of loading scenarios. These instabilities initiate large *dynamic* responses which may also produce nonlinear transitions to more energetically favorable equilibria. Very few studies [10-15] have developed dynamic rod models sufficient for describing the dynamic evolution of loops. The dynamic model in [15] is artificially damped to study the quasi-static evolution of self-contact and intertwining in biological filaments, while those in [10-14] capture dynamic responses of underwater cables with hydrodynamic forces [16] but without self-contact.

All of the above formulations assume the rod to be isotropic and homogeneous. These assumptions fall short when considering the mechanics of synthetic and wire rope cables where anisotropy arises due to their helical construction [17]. The helical construction couples tensile (or compressive) and torsional stresses [18]. Many underwater cables are also intentionally non-homogeneous. For example, S-tethers (see Fig. 2) are designed with segments of different materials (with different buoyancy) to create considerable slack [19]. The first generic dynamic cable model that captures all the above features was developed by Goyal et al. [20-22].

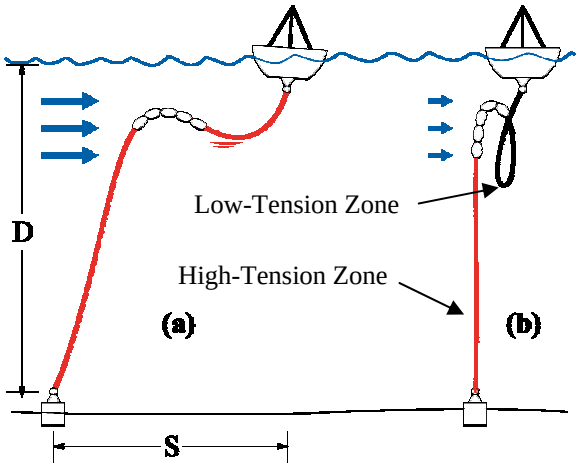


**Fig. 2**: Loop formation in slack zone of S-tether.

The computational model [20] captures the mechanics of low-tension cables by using a rod theory in the form of a 12th order system of partial differential equations. In many underwater cable applications such as depicted in Figs. 1 and 2, however, the low tension zone is confined to a very small fraction of the computational domain rendering the use of a rod model for the entire cable both computationally inefficient and unnecessary. The dynamics of high-tension zones can be efficiently described using a 6th order flexible "catenary". An example of 6th order catenary element was employed by Howell [23] to investigate the dynamics of hanging chains.

In this paper, we contribute an efficient computational cable model that exploits distinct formulations in low- versus high-tension zones. While it is necessary to use a (12th order) rod model to resolve the low tension regions and the possible formation loops and tangles, we then employ a (6th order) catenary model for the remainder of the computational domain where tension effects dominate the effects of flexure and torsion. The resulting hybrid cable model adaptively transitions between rod and catenary elements contingent on the relative importance of tension versus bending and/or torsion in any sub-domain. An example of this approach appears in the analytical formulation of Kevorkian and Cole [24] who employ singular perturbation to blend linear beam and string formulations to understand the local effects of bending in an otherwise long and taut string. Another example appears in Sun and Leonard [10] who proposed a hybrid computational model of fluid-loaded cables that blends rod and catenary formulations through a point discontinuity. Herein, we use a similar strategy to blend the computationally efficient rod model described in [20] with the catenary model employed in [23].

We open in Section 2 by reviewing the governing equations of the dynamical rod theory from Goyal et al. [20] and the catenary theory from Howell [23]. We join the two models by means of a spherical joint. In Section 3, we extend the efficient finite difference method used in [20] (that employs the generalized-α method [12, 14, 25] in both space and time) to this hybrid rod-catenary model. In Section 4, we test the hybrid model for a simple cable suspension that involves low and high tension zones. We validate the hybrid model by benchmarking results with those obtained from a pure (computationally expensive) rod model. We close with conclusions in Section 5.

## 2. THE CATENARY AND ROD MODELS

The three-dimensional curve formed by the cable centerline is parameterized by the arc-length coordinate $s$ and time $t$. The centerline is divided into sub-domains of rod and catenary elements. We adopt the rod model from Goyal et al. [20] and the catenary model from Howell [23]. The governing equations for each model are summarized below.

### 2.1 *Governing Equations for a Catenary*

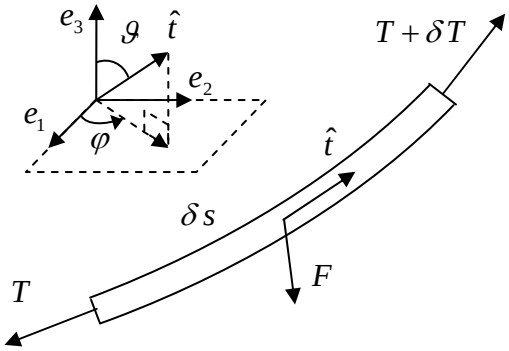


**Fig. 3**: Free body diagram of an infinitesimal element of a catenary.

The deformation of catenary (see Fig. 3) is determined solely by the orientation of centerline tangent $\hat{t}(s,t)$ and the extensional strain $\varepsilon(s,t)$ [1]. The strain is related to the tension $T(s,t)$ in the catenary through the compliance $c_k(s)$,

$$\varepsilon(s,t) = c_k(s)T(s,t). \tag{1}$$

The field equations[2] for the catenary are:

$$\frac{\partial v}{\partial s} = \frac{\partial}{\partial t}\left\{(1+\varepsilon)\hat{t}\right\}, \tag{2}$$

[1] The arc-length co-ordinate $S$ is assumed to correspond to that for the unstretched state.

[2] Equation (2) results from the continuity of the (extensible) centerline and Eq. (3) results from balance of linear momentum.

$$\hat{t}\frac{\partial T}{\partial s} + T\frac{\partial \hat{t}}{\partial s} + F = m\frac{\partial v}{\partial t}, \quad (3)$$

where $m(s)$ denotes the mass per unit arc length, $F(s,t)$ denotes the distributed force[3] per unit arc length, and $v(s,t)$ denotes the velocity of the centerline. All derivatives are relative to the inertial frame $\{e_i\}$. The unit vector $\hat{t}$ can be parameterized by its two spherical co-ordinates (see Fig. 3) $\vartheta(s,t)$ and $\varphi(s,t)$ such that its components along $\{e_i\}$ become

$$\hat{t} = \begin{bmatrix} \sin\vartheta\cos\varphi & \sin\vartheta\sin\varphi & \cos\varphi \end{bmatrix}. \quad (4)$$

Substituting Eq. (1) and Eq. (4) in Eqs. (2-3), yields a 6th order system of partial differential equations in the field variables $Y_c = \begin{bmatrix} v & T & \vartheta & \varphi \end{bmatrix}$,

$$M_c(Y_c,s,t)\frac{\partial Y_c}{\partial t} + K_c(Y_c,s,t)\frac{\partial Y_c}{\partial s} + F_c(Y_c,s,t) = 0, \quad (5)$$

where matrices $M_c$, $K_c$ and $F_c$ are as defined in Appendix 2.

### 2.2 *Governing Equations for a Rod*

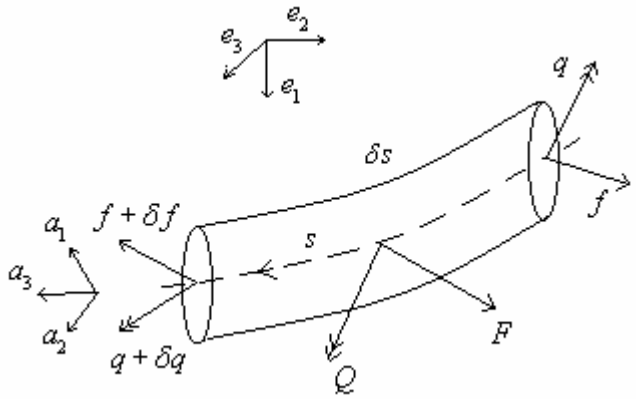


**Fig. 4**: Free body diagram of an infinitesimal element of a rod.

The rod element (see Fig. 4) employs a body-fixed frame $\{a_i\}$ at each cross-section to describe its orientation with respect to the inertial frame $\{e_i\}$. The deformation field is represented by the curvature and twist vector $\kappa(s,t)$ that is defined by the rotation per unit arc length of the body-fixed frame. The curvature and twist $\kappa(s,t)$ results in the internal moment $q(s,t)$ in rod element that obeys an (assumed) linear elastic constitutive law:

$$q(s,t) = B(s)\kappa(s,t) \quad (6)$$

where the tensor $B(s)$ captures the stiffness of the rod in bending and torsion. The rod is assumed to be unshearable and inextensible, but can sustain shear and tensile stresses resulting in the internal force $f(s,t)$.

The field equations[4] for the rod are:

$$\frac{\partial v}{\partial s} + \kappa \times v = \omega \times \hat{t}, \quad (7)$$

$$\frac{\partial \omega}{\partial s} + \kappa \times \omega = \frac{\partial \kappa}{\partial t}, \quad (8)$$

$$\frac{\partial q}{\partial s} + \kappa \times q = I\frac{\partial \omega}{\partial t} + \omega \times I\omega + f \times \hat{t} - Q, \quad (9)$$

$$\frac{\partial f}{\partial s} + \kappa \times f = m\left(\frac{\partial v}{\partial t} + \omega \times v\right) - F, \quad (10)$$

where $\omega(s,t)$ denotes the cross-section angular velocity, $I(s)$ denotes the tensor of principal mass moments of inertia per unit arc length, $Q(s,t)$ denotes the distributed moment per unit arclength and the remaining variables/ parameters are as in the catenary model. The partial derivatives are all relative to the body-fixed frame $\{a_i\}$.

Equations (7-10) result[5] in a 12th order system of partial differential equations in the field variables $Y_r = \begin{bmatrix} v & \omega & \kappa & f \end{bmatrix}$,

$$M_r(Y_r,s,t)\frac{\partial Y_r}{\partial t} + K_r(Y_r,s,t)\frac{\partial Y_r}{\partial s} + F_r(Y_r,s,t) = 0, \quad (11)$$

where matrices $M_r$, $K_r$ and $F_r$ are as defined in Appendix 2.

### 2.3 *Constraints at a Rod-Catenary Interface*

The rod and catenary elements must now be joined in such a manner that preserves continuity of the displacement (velocity) field and also force and moment equilibrium. These requirements are achieved by introducing a spherical joint at rod-catenary interface. In the formulation above, the catenary variables are represented with components in the inertial frame $\{e_i\}$, while the rod variables are represented with components in the body-fixed frame $\{a_i\}$. Let $L(s,t)$ denote the tensor that transforms a vector from the inertial frame to the body-

[3] The distributed force is used to capture buoyant weight and hydrodynamic drag as detailed in Appendix 1.

[4] Equation (7) is the inextensibility constraint, Eq. (8) is a compatibility condition, and Eqs. (9-10) are the Newton-Euler equations for an infinitesimal rod element.

[5] Substitute Eq. (6) into Eq. (9). Also recognize that the tangent vector $\hat{t}$ is constant in the body-fixed frame $\{a_i\}$ for an unshearable rod and points along the principal axis for torsion.

fixed frame. If the joint is located at $s = s_j$ along the cable centerline, then the above interface conditions become

$$q_r(s_j,t) = 0 \Rightarrow \kappa_r(s_j,t) = 0\,, \tag{12}$$

$$v_r(s_j,t) = L_r(s_j,t)v_c(s_j,t)\,, \tag{13}$$

$$f_r(s_j,t) = L_r(s_j,t)\hat{t}_c(s_j,t)T_c(s_j,t)\,, \tag{14}$$

where the subscripts $r$ and $c$ identify rod and catenary variables, respectively.

Note that the tangent to the catenary $\hat{t}_c(s_j,t)$ need not align with the tangent to the rod $\hat{t}_r(s_j,t)$ at the spherical joint interface. A seemingly better choice may appear from imposing continuity of curvature and geometric torsion in lieu of the "moment-free" condition above. However, recall that the catenary cannot sustain any internal moment. Thus, the catenary simply cannot be used in subdomains where appreciable curvature and/or torsion are likely to arise, as in the low tension regions. The above transition from catenary to rod must occur at (or before) the earliest appearance of curvature and torsion as determined by an acceptably small threshold, and the simple moment-free spherical joint remains appropriate for this transition.

## 3. NUMERICAL ALGORITHM

Equation (5) is a 6th order initial-boundary value problem that requires 3 boundary conditions at the two boundary points of the catenary. Similarly Eq. (12) is a 12th order initial-boundary value problem that requires 6 boundary conditions at the two boundary points of the rod. At the rod-catenary interface, the 9 constraints of the spherical joint given by Eqs. (12-14) substitute for the (6+3) boundary conditions required by each rod and catenary models.

For integration of the initial-boundary value problem, we employ the generalized-α method [12, 14, 25] in both space and time. The resulting implicit algorithm is 2nd order accurate, unconditionally stable, and incorporates a (controllable) numerical dissipation parameter. Starting with the initial value $Y(s,0)$, the discretized equations are integrated over space at each successive time step. The boundary conditions are satisfied during spatial integration using a shooting method for boundary-value problems as detailed in [13].

The boundary conditions and distributed forces/moments are often most readily decomposed into components in the inertial frame. During integration, these components must be transformed to those in the body fixed frame for rod through the transformation matrix $L(s,t)$. Standard formulations employ three Euler angles or four Euler parameters to construct the nine components of $L(s,t)$. Here, we employ incremental rotations [26]. Accordingly, we compute the small change in $L(s,t)$ through the time step $\Delta t$ using the small incremental rotation $\Phi(s,t,t-\Delta t)$

$$L(s,t) = \Phi(s,t,t-\Delta t)L(s,t-\Delta t)\,. \tag{15}$$

The incremental rotation can be accomplished through a single rotation (about one axis) as per Euler rotation theorem [27]. Let the vector $\theta(s,t)$ represent the (axis and amount of) the single infinitesimal rotation for $\Phi(s,t,t-\Delta t)$. Then

$$\omega(s,t) = \lim_{\Delta t \to 0} \frac{\theta(s,t)}{\Delta t} \quad \text{and} \quad \Phi = \exp(-\tilde{\theta})\,, \tag{16}$$

where $\tilde{\theta}$ is the skew-symmetric form of $\theta$ defined as follows. The cross product of two vectors $x$ and $y$ can be written as $x \times y = \tilde{x}y$, where

$$x = \begin{Bmatrix} x_1 \\ x_2 \\ x_3 \end{Bmatrix}, y = \begin{Bmatrix} y_1 \\ y_2 \\ y_3 \end{Bmatrix}, \tilde{x} = \begin{bmatrix} 0 & -x_3 & x_2 \\ x_3 & 0 & -x_1 \\ -x_2 & x_1 & 0 \end{bmatrix}. \tag{17}$$

The exponential of skew-symmetric matrix $\tilde{x}$ is expanded as

$$\exp(\tilde{x}) = \mathrm{I} + \tilde{u}\sin(|x|) + \tilde{u}^2(1-\cos(|x|)), \tag{18}$$

where $|x|$ is the magnitude of $x$, $u$ is the unit vector along $x$ and $\mathrm{I}$ is the identity matrix. Note that this computation employs only a scalar power series and it therefore avoids the known numerical difficulties of matrix exponentiation [28].

In short, we use (16) to compute $\theta(s,t)$ and $\Phi(s,t,t-\Delta t)$ and then use (15) to update $L(s,t)$. From the transformation matrix $L(s,t)$ and the centerline velocity $v(s,t)$, we then compute the position and orientation of each cross section of the rod at any time by subsequent integration. For the catenary, we need to integrate only $v(s,t)$ to compute the evolution of its shape in time.

## 4. RESULTS AND DISCUSSION

The principal contribution of this paper lies in the formulation of the hybrid rod-catenary formulation described in Sections 2 and 3. In this section, we evaluate the performance of the hybrid rod-catenary model using a relatively simple example featuring a cable suspension with both low and high tension zones. We validate the hybrid model by benchmarking results with those obtained from a pure rod model.

The example is illustrated in Fig. 5 and corresponding parameters are listed in Table 1. The figure shows a cable of length $L$ sagging under its own weight. The left end is pinned. At the right end, the cable centerline is given a prescribed orientation of 30 degrees from the horizontal, is tension-free, but subject to an applied force in the normal (shear) direction. A reaction moment also develops at the right end in response to prescribing the rotation of this end and leads to a region where significant curvature develops.

**Table 1:** Simulation parameters.

| *Quantity* | *Symbol* | *Units (SI)* | *Value* |
|---|---|---|---|
| **I. CABLE** | | | |
| Diameter | $D$ | m | $1.0\times10^{-3}$ |
| Length | $L$ | m | $2.0\times10^{0}$ |
| Mass/ length | $m$ | Kg/m | $\pi/4\times10^{-3}$ |
| Bending Moment of Inertia/ length | Tensor $I$ | Kg-m | $\pi/64\times10^{-9}$ |
| Torsional Moment of Inertia/ length | | Kg-m | $\pi/32\times10^{-9}$ |
| Bending Stiffness | Tensor $B$ | N-m$^2$ | $5\pi/64\times10^{-3}$ |
| Torsional Stiffness | | N-m$^2$ | $\pi/16\times10^{-3}$ |
| Compliance | $c_k$ | N$^{-1}$ | $0.0\times10^{0}$ |
| **II. FLUID ENVIRONMENT (See Appendix 1)** | | | |
| Acceleration due to gravity | $g$ | m/s$^2$ | $9.8\times10^{0}$ |
| Fluid Density | $\rho_f$ | Kg/m$^3$ | $1.0\times10^{0}$ |
| Normal Drag Coefficient | $C_n$ | - | $1.0\times10^{0}$ |
| Tangential Drag Coefficient | $C_t$ | - | $1.0\times10^{-1}$ |
| Added Fluid Mass | $m_a$ | Kg | $0.0\times10^{0}$ |
| Far-field flow | $v_f$ | m/s | $0.0\times10^{0}$ |
| Applied Boundary Force (Fig. 5) | $f_{applied}$ | N | $1.0\times10^{-2}$ |
| **III. NUMERICAL DISCRETIZATION** | | | |
| Temporal Step | - | s | $1.0\times10^{0}$ |
| Spatial Step | - | m | $5.0\times10^{-3}$ |
| Joint Location | $s_j$ | m | $1.5\times10^{0}$ |

Two computational models are used to predict the dynamic relaxation to equilibrium from an initially straight cable. The first is the pure rod model (dashed curve) while the second is the hybrid rod-catenary model (solid curve) composed of 25% rod-domain (black) and 75% catenary sub-domain (red). The rod sub-domain is joined to the catenary sub-domain at point $s_j$ with a spherical joint. While the two models predict similar displacements, the modest differences arise from the added flexibility of the hybrid model as seen, for instance by comparing the maximum sag. More importantly, there is a significant increase in the calculation speed for the hybrid model in proportion to the ratio of the catenary/rod sub-domains. For example, under equal conditions, the computational speed is increased by approximately a factor of 1.5 to 2 for this very simple example when using the hybrid model. In addition, the hybrid model successfully captures the mechanics of bending at the right end that would otherwise be missed in a pure catenary model as described further below.

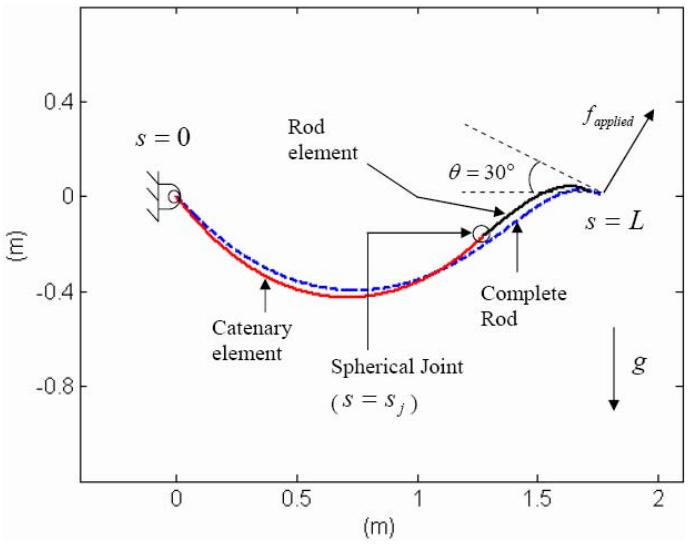


**Fig. 5**: A simple benchmark example: a cable suspension with low (black) and high (red) tension zones.

The force and moment distributions along the cable obtained from the two computational models are compared in Figs. 6-8. The tension distribution shown in Fig. 6 demonstrates that the steady-state tension predicted by the hybrid model closely matches that of the rod model. This is certainly expected as the catenary successfully captures the tension-dominated mechanics of a cable. The tension is continuous across the rod/catenary interface and there remains only a very minute tension gradient in the rod subdomain to the right of this interface. Moreover, the tension in the rod subdomain eventually decreases to zero at the right end as required by the boundary condition. The resulting low-tension (rod) subdomain develops appreciate bending.

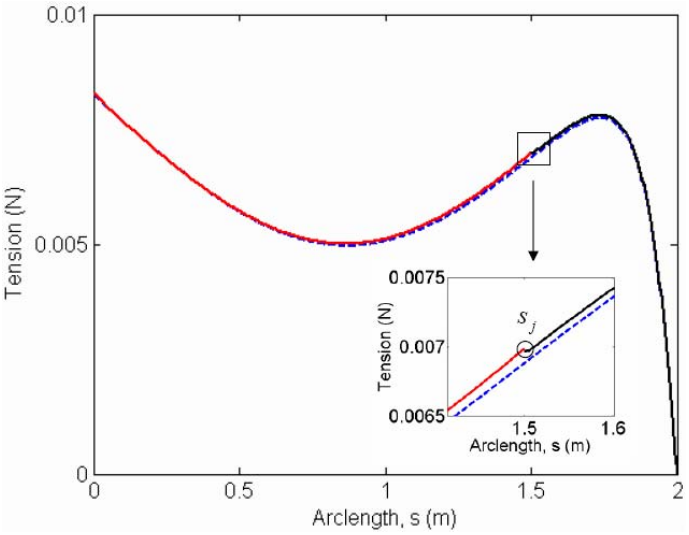


**Fig. 6**: Final tension distribution.

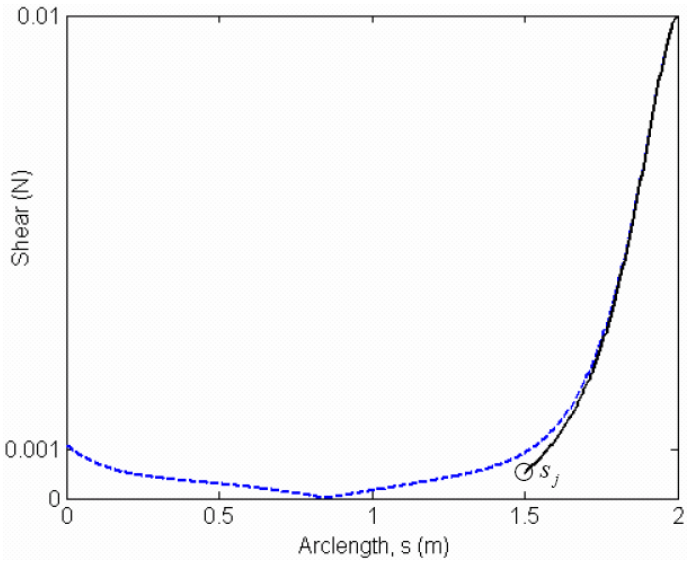


**Fig. 7**: Final shear force distribution.

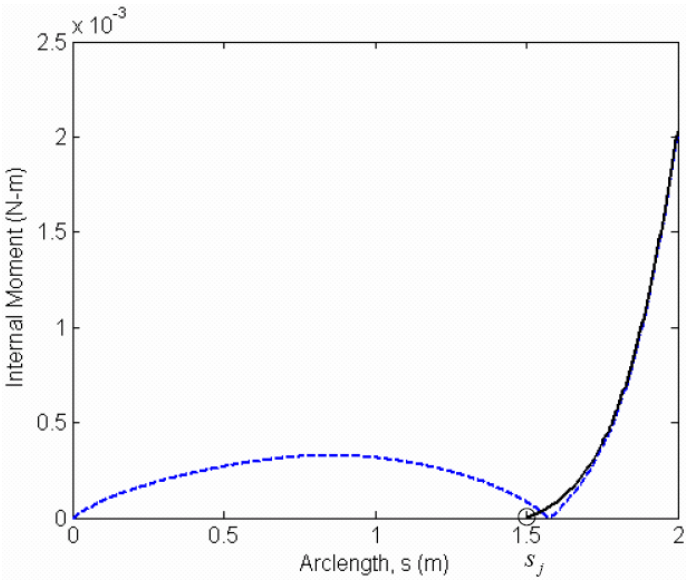


**Fig. 8**: Final internal moment distribution.

The shear force and bending moment in hybrid model in Figs. 7 and 8 are reported only in the rod sub-domain as these quantities vanish in the catenary sub-domain. Note also that the shear force and bending moments for the pure rod model remain relatively small values in the corresponding domain ($s < s_j$) where the catenary was employed in the hybrid model. In addition, the hybrid model accurately reproduces the shear and bending moment in the rod subdomain as benchmarked against the pure rod solution.

## 5. CONCLUSIONS

The main contribution of this paper is the formulation of a hybrid rod-catenary model to efficiently compute the dynamics of long cables that possess both low and high tension subdomains. Such tension changes arise in ocean engineering cables, as seen for example, in S-tether moorings and in cases of cable/seabed contact. Pure rod models ultimately lead to ill-conditioned computations for the very flexible, long cables often used in ocean engineering applications. Pure catenary models are well-known to be ill-conditioned for low tension cables. Thus, it is natural to employ these models in opposite tension regimes; that is, employ the rod model in low tension subdomains, and employ the catenary model in high tension subdomains. The hybrid model herein inherits the computational benefits of each model and offers tremendous computational advantages. For the simple cable suspension chosen as an example herein, the hybrid model increases computational speed by a factor of 1.5-2 relative to the pure rod model. In addition, the hybrid model successfully captures the dominant effects of bending in the low tension region that would otherwise be lost in using a pure catenary model.

## ACKNOWLEDGMENTS

The authors gratefully acknowledge the research support provided by the U. S. Office of Naval Research.

## REFERENCES

[1] Love, A.E.H., 1944, *A Treatise on the Mathematical Theory of Elasticity*, Dover Publications, New York.
[2] Antman, S.S., 2004, *Nonlinear Problems in Elasticity*, Springer-Verlag, New York.
[3] Timoshenko, S.P., and Gere, J.M., 1961, *Theory of Elastic Stability*, McGraw-Hill, New York.
[4] Zachmann, D.W., 1979, "Non-Linear Analysis of a Twisted Axially Loaded Elastic Rod," Quarterly of Applied Mathematics, **37**, pp. 67-72.
[5] Zajac, E.E., 1962, "Stability of Two Planar Loop Elasticas," ASME J. of Applied Mechanics, **29**, pp. 136-142.
[6] Coyne, J., 1990, "Analysis of the Formation and Elimination of Loops in Twisted Cable," IEEE J. of Oceanic Engineering, **15**, pp. 72-83.
[7] Rosenthal, F., 1976, "Application of Greenhills Formula to Cable Hockling," ASME J. of Applied Mechanics, **43**, pp. 681-683.
[8] Lu, C.L., and Perkins, N.C., 1995, "Complex Spatial Equilibria of U-Joint Supported Cables under Torque, Thrust and Self-Weight," International J. of Non-Linear Mechanics, **30**, pp. 271-285.
[9] van der Heijden, G.H.M., Neukirch, S., Goss, V.G.A., and Thompson, J.M.T., 2003, "Instability and Self-contact Phenomena in the Writhing of Clamped Rods," International J. of Mechanical Sciences, **45**, pp. 161-196.
[10] Sun, Y., and Leonard, J.W., 1998, "Dynamics of Ocean Cables with Local Low-Tension Regions," Ocean Engineering, **25**, pp. 443-463.
[11] Gatti-Bono, C., and Perkins, N.C., 2002, "Dynamic Analysis of Loop Formation in Cables under Compression," International J. of Offshore and Polar Engineering, **12**, pp. 217-222.
[12] Gobat, J.I., Grosenbaugh, M.A., and Triantafyllou, M.S., 2002, "Generalized-Alpha Time Integration Solutions for Hanging Chain Dynamics," ASCE J. of Engineering Mechanics, **128**, pp. 677-687.

[13] Gatti-Bono, C., and Perkins, N.C., 2002, "Physical and Numerical Modelling of the Dynamic Behavior of a Fly Line," ASME J. of Sound and Vibration, **255**, pp. 555-577.
[14] Gobat, J.I., and Grosenbaugh, M.A., 2001, "Application of the Generalized-Alpha Method to the Time Integration of the Cable Dynamics Equations," Computer Methods in Applied Mechanics and Engineering, **190**, pp. 4817-4829.
[15] Klapper, I., 1996, "Biological Applications of the Dynamics of Twisted Elastic Rods," J. of Computational Physics, **125**, pp. 325-337.
[16] Morison, J.R., O'Brien, M.P., Johnson, J.W., and Schaaf, S.A., 1950, "The Force Exerted by Surface Waves on Piles," Transactions of the American Institute of Mining and Metallurgical Engineers, **189**, pp. 149-154.
[17] Costello, G.A., 1997, *Theory of Wire Rope*, Springer-Verlag, New York.
[18] Healey, T.J., 2002, "Material Symmetry and Chirality in Nonlinearly Elastic Rods," Mathematics and Mechanics of Solids, **7**, pp. 405-420.
[19] Han, S., and Grosenbaugh, M.A., 2003, "On the Design of S-Tethor Oceanographic Moorings," *Proc., 13th International Offshore and Polar Engineering Conference*, Honolulu, Hawaii, USA.
[20] Goyal, S., Perkins, N.C., and Lee, C.L., "Nonlinear Dynamics and Loop Formation in Kirchhoff Rods with Implications to the Mechanics of DNA and Cables" J. of Computational Physics, (in Press 2005).
[21] Goyal, S., Perkins, N.C., and Lee, C.L., 2003, "Writhing Dynamics of Cables with Self-contact," *Proc., 5th International Symposium of Cable Dynamics*, Santa Margherita Ligure, Italy.
[22] Goyal, S., Perkins, N.C., and Lee, C.L., 2003, "Torsional Buckling and Writhing Dynamics of Elastic Cables and DNA," *Proc., 2003 ASME Design Engineering Technical Conferences and Computers and Information in Engineering Conference*, Chicago, IL, United States.
[23] Howell, C.T., 1992, "Investigation of Large Amplitude Nonlinear Dynamics of Hanging Chains," Proc., 2nd International Offshore and Polar Engineering Conference, San Francisco, United States.
[24] Kevorkian, J., and Cole., J.D., 1985, *Perturbation Methods in Applied Mathematics*, Springer-Verlag, New York.
[25] Chung, J., and Hulbert, G.M., 1993, "A Time Integration Algorithm for Structural Dynamics with Improved Numerical Dissipation - The Generalized-Alpha Method," ASME J. of Applied Mechanics,. **60**, pp. 371-375.
[26] Bottasso, C.L., and Borri, M., 1998, "Integrating Finite Rotations," Computer Methods in Applied Mechanics and Engineering, **164**, pp. 307-331.
[27] Nikravesh, P.E., 1988, *Computer-aided Analysis of Mechanical Systems*, Prentice-Hall, Englewood Cliffs.
[28] Moler, C., and Vanloan, C., "19 Dubious Ways to Compute Exponential of a Matrix," SIAM Review, 1978. **20**(4): p. 801-836.

## APPENDIX 1: HYDRODYNAMICS

The hydrodynamics of underwater cables is dominated by fluid inertia (high Reynolds number) and is effectively modeled with standard Morison drag and added mass effects [16] for a cylinder in the far-field flow $v_f$:

$$F_{drag} = \frac{1}{2}\rho_f D\left\{C_n\left|v_r \times \hat{t}\right|\hat{t}\times\left(v_r\times\hat{t}\right)+\pi C_t\left(v_r\cdot\hat{t}\right)\left|v_r\cdot\hat{t}\right|\hat{t}\right\}, \tag{19}$$

$$F_{added\_mass} = -m_a\frac{\partial v}{\partial t}. \tag{20}$$

Here $v_r = v_f - v$ is the flow relative to the cable, $\rho_f$ is the fluid density, $D$ is the cable diameter, $C_n$ and $C_t$ are the normal (form) drag and tangential (skin friction) drag coefficients respectively and $m_a$ is the added fluid mass. The partial differentiation is relative to the inertial frame $\{e_i\}$. The cable buoyant weight per unit length is

$$F_{buoyant\_weight} = \left(m - \rho_f\frac{\pi D^2}{4}\right)g, \tag{21}$$

where $m$ is the cable mass per unit length and the vector $g$ is the acceleration due to gravity. The forces (per unit length) $F_{drag}$, $F_{added\_mass}$ and $F_{buoyant\_weight}$ are included in the hybrid rod-catenary model through the distributed force term $F$ in the linear momentum equation, Eq. (3) for the catenary sub-domain, and Eq. (10) for the rod sub-domain. For an extensible catenary, assuming $D$ does not change appreciably, the net external force/length becomes

$$F = (F_{drag} + F_{added\_mass})(1+\varepsilon) + F_{buoyant\_weight}, \tag{22}$$

Here, $\varepsilon$ follows from Eq. (1), the hydrodynamic forces $F_{drag}$ and $F_{added\_mass}$ from Eq. (15) and Eq. (16), and the buoyant weight from

$$F_{buoyant\_weight} = \left(m - \rho_f\frac{\pi D^2}{4}(1+\varepsilon)\right)g, \tag{23}$$

## APPENDIX 2: COEFFICIENT MATRICES

Let $\Theta$ be the $3\times3$ null matrix and $\mathrm{I}$ be the $3\times3$ identity matrix. The coefficient matrices used in Eq. (5) and Eq. (11) are:

$$M_c = \begin{bmatrix} \Theta & \tilde{M} \\ m\mathrm{I} & \Theta \end{bmatrix},$$
$$\tilde{M} = \begin{bmatrix} c_k \hat{t} & (1+c_k T)\dfrac{\partial \hat{t}}{\partial \vartheta} & (1+c_k T)\dfrac{\partial \hat{t}}{\partial \varphi} \end{bmatrix}_{3\times 3} \tag{24}$$

$$K_c = -\begin{bmatrix} \mathrm{I} & \Theta \\ \Theta & \tilde{K} \end{bmatrix},$$
$$\tilde{K} = \begin{bmatrix} \hat{t} & T\dfrac{\partial \hat{t}}{\partial \vartheta} & T\dfrac{\partial \hat{t}}{\partial \varphi} \end{bmatrix}_{3\times 3} \tag{25}$$

$$F_c = \begin{Bmatrix} 0 \\ 0 \\ 0 \\ -F \end{Bmatrix}. \tag{26}$$

The partial derivatives in Eq. (24) and Eq. (25) are relative to the inertial frame $\{e_i\}$.

$$M_r = \begin{bmatrix} \Theta & \Theta & \Theta & \Theta \\ \Theta & \Theta & \mathrm{I} & \Theta \\ \Theta & I & \Theta & \Theta \\ m\mathrm{I} & \Theta & \Theta & \Theta \end{bmatrix} \tag{27}$$

$$K_r = -\begin{bmatrix} \mathrm{I} & \Theta & \Theta & \Theta \\ \Theta & \mathrm{I} & \Theta & \Theta \\ \Theta & \Theta & B & \Theta \\ \Theta & \Theta & \Theta & \mathrm{I} \end{bmatrix} \tag{28}$$

$$F_r = \begin{Bmatrix} \omega \times \hat{t} - \kappa \times v \\ -\kappa \times \omega \\ -\dfrac{\partial B}{\partial s}\kappa + \omega \times I\omega + f \times \hat{t} - \kappa \times B\kappa - Q \\ m(\omega \times v) - \kappa \times f - F \end{Bmatrix}. \tag{29}$$

The partial derivative $\dfrac{\partial B}{\partial s}$ in Eq. (29) is relative to the body-fixed frame $\{a_i\}$.